Large eddy simulation of a plane jet

C. Le Ribault, S. Sarkar, and S. A. Stanley

Articles you may be interested in

Assessment of subgrid-scale models with a large-eddy simulation-dedicated experimental database: The pulsatile impinging jet in turbulent cross-flow
Phys. Fluids **26**, 075108 (2014); 10.1063/1.4890855

Large-eddy simulation of highly underexpanded transient gas jets
Phys. Fluids **25**, 016101 (2013); 10.1063/1.4772192

Large-eddy simulation of the flow and acoustic fields of a Reynolds number 10 5 subsonic jet with tripped exit boundary layers
Phys. Fluids **23**, 035104 (2011); 10.1063/1.3555634

On using large-eddy simulation for the prediction of noise from cold and heated turbulent jets
Phys. Fluids **17**, 085103 (2005); 10.1063/1.2001689

Large eddy simulation of a plane turbulent wall jet
Phys. Fluids **17**, 025102 (2005); 10.1063/1.1833413

Large eddy simulation of a plane jet

C. Le Ribault
Laboratoire de Mécanique des Fluids et d'Acoustique, Ecole Centrale de Lyon, 69130, Ecully, BP163, France

S. Sarkar and S. A. Stanley[a]
Department of AMES, University of California, San Diego, La Jolla, California 92093-0411

Large eddy simulations of spatially evolving planar jets have been performed using the standard Smagorinsky, the dynamic Smagorinsky, and the dynamic mixed models and model performance evaluated. Computations have been performed both at a low Reynolds number, $Re_d = 3000$, in order to make comparisons with a previous DNS at the same Reynolds number, and at a higher value, $Re_d = 30\,000$, to compare with high Reynolds number experiments. Model predictions with respect to the evolution of jet half-width, centerline velocity decay, mean velocity profiles, and profiles of turbulence intensity are evaluated. Some key properties of the SGS models such as the eddy-viscosity constant and the subgrid dissipation are also compared. It is found that the standard Smagorsinsky model is much too dissipative and severely underpredicts the evolution of the jet half-width and centerline velocity decay. The dynamic versions of the Smagorinsky model and the mixed model allow for streamwise and transverse variation of the constant in the eddy-viscosity expression which results in much better performance and good agreement with experimental and DNS data. The mixed model has an additional scale-similarity part which, in *a priori* tests against filtered jet DNS data, is found to predict the subgrid shear stress profile. Although the subgrid shear stress obtained by the dynamic Smagorinsky model is substantially smaller than that obtained in the *a priori* tests using the jet DNS data, surprisingly, in the *a posteriori* computations, the dynamic Smagorinsky model performs as well as the dynamic mixed model. Analysis of the mean momentum equation gives the reason for such behavior: the resolved stress in computations with the dynamic Smagorinsky model is larger than it should be and compensates for the underprediction of the subgrid shear stress by the Smagorinsky model. The numerical discretization errors have been quantified. The error due to noncommutativity of spatial differentiation and physical space filtering on nonuniform grids is found to be small because of the relatively mild stretching used in the present LES. The modeling error is found to be generally smaller than the discretization error with the standard Smagorinsky model having the largest modeling error. © *1999 American Institute of Physics.* [S1070-6631(99)04409-8]

I. INTRODUCTION

Jets in complex configurations are typically encountered in different practical engineering applications such as combustors, cooling of energy conversion devices, and exhaust of aerospace vehicles, as well as in environmental problems. It is then important to understand the physics related to modeling a simple jet to improve prediction methods in more complex flows. The purpose of this study is to investigate the ability of large eddy simulation (LES) to predict the overall field quantities in the plane jet and the evolution of the two initial shear layers upstream to the jet.

Many experimental studies and results are available on jets.[1–13] Characteristics in the near field of the jet nozzle as well as in the self-preservation region have been investigated. Large statistical structures are seen, especially in the near field, that include a Von Karman vortex street and rollerlike structures. The works of Antonia *et al.*[1] and Thomas and Prakash[2] have shown that, near the nozzle, the structures are predominantly symmetrical for a flat exit profile. After the merging of the shear layers, asymmetric structures appear in the fully developed region of the jet. The self-preserving region of the jet is characterized by linear growth of its thickness, quadratic decay of the centerline velocity, and constant values of the centerline turbulence intensities, when normalized by the centerline velocity. The ability of LES to give quantitatively correct predictions of these quantities is of interest.

Many jet numerical simulations have also been performed but most of them have involved temporally evolving jets as well as a round geometry. Fewer simulations have been performed of spatially evolving jets because of the high computational cost. A large eddy simulation of a round jet has been performed by Urbin and Metais[14] that focuses on the coherent vortex dynamics. Coannular jets discharging into a sudden expansion region have been studied by Akselvoll and Moin.[15] Recent large eddy simulations of a plane jet have also been performed by Dai *et al.*[16] and Weinberger *et al.*[17] to investigate the influence of the inlet conditions on

[a]Present address: Lawrence Berkeley National Laboratory, 50A-1148, Berkeley, CA 94720.

the jet. Both simulations were restricted to the standard Smagorinsky model.

In direct simulations, the Navier–Stokes equations are solved and all dynamically important scales of turbulence are computed. Such computations are very accurate but require very refined meshes and small time steps. In large eddy simulation only the largest scales are simulated and the effect of small scales on the large resolved scales is modeled. LES requires less computational effort and can simulate flows at higher Reynolds number than direct numerical simulation (DNS). An accurate DNS of a spatially evolving jet with a low co-flow (strong jet) has been performed by Stanley and Sarkar.[18] The simulation studies the evolution of the initial shear layers at the jet edge, their merging at the end of the potential core, and, finally, the well-developed jet. The DNS results[18] are in good agreement with experimental results.

In the present work, large eddy simulation of a planar jet is performed. Unlike the previous LES studies of the plane jet, the dynamic Smagorinsky model and the mixed model are used in addition to the Smagorinsky model and their performance evaluated. Furthermore, the LES results are validated against both DNS and experiments. In the first part of the study, computations at the same Reynolds number as the direct numerical simulation are performed in order to compare the results and validate the method. In the second part, the Reynolds number of the jet is increased and compared with higher Reynolds number experiments.

II. GOVERNING EQUATIONS

A. Navier–Stokes equations

The flow is governed by the Navier–Stokes equations, representing mass conservation,

$$\partial_t \rho + \partial_i(u_i \rho) = 0, \tag{1}$$

momentum conservation,

$$\partial_t(\rho u_i) + \partial_j(\rho u_i u_j) = -\partial_i p + \frac{1}{\text{Re}} \partial_j \tau_{ij}, \tag{2}$$

and energy conservation written as an evolution equation for the pressure field,

$$\partial_t p + u_i \, \partial_i p + \gamma p \, \partial_i u_i = \frac{\gamma}{\text{Pr Re}} \partial_i(k \partial_i T) + \frac{\gamma - 1}{\text{Re}} \tau_{ij} \, \partial_i u_j. \tag{3}$$

The tensor τ_{ij} represents the viscous stress:

$$\tau_{ij} = \mu(\partial_j u_i + \partial_i u_j) - \tfrac{2}{3} \mu \, \delta_{ij} \, \partial_k u_k. \tag{4}$$

In the above equations, Re is the Reynolds number and Pr the Prandtl number. Although the compressible Navier–Stokes equations are used for future generalization to high-speed flow, the jet Mach number, $M_j = 0.3$, is sufficiently small that compressibility effects may be neglected.

B. Filtered equations

In DNS, Eqs. (1)–(3) are directly solved without further modeling. To reduce the required numerical resolution, the Navier–Stokes equations in the LES approach are filtered. Therefore, the small scales are not directly solved for in LES

but modeled. In this paper, the top-hat filter with a filter width Δ is used. Three filter sizes are tested: $\Delta = h$ where h represents the grid spacing, $\Delta = 2h$, and $\Delta = 4h$. A filtering operation weighted by the density ρ is used following the approach used by Favre for compressible flows:

$$\tilde{f} = \overline{\rho f}/\bar{\rho}. \tag{5}$$

The filtered Navier–Stokes equations, that have been, for example, developed in Lesieur and Comte,[19] are as follows:

$$\partial_t \bar{\rho} + \partial_j(\bar{\rho} \tilde{u}_j) = 0, \tag{6}$$

$$\partial_t(\bar{\rho} \tilde{u}_i) + \partial_j(\bar{\rho} \tilde{u}_i \tilde{u}_j) + \partial_i \bar{p} = \frac{1}{\text{Re}} \partial_j(\overline{\tau_{ij}}) - \partial_j \bar{\rho} q_{ij} + R_m, \tag{7}$$

$$\partial_t \bar{p} + \overline{u_i} \, \partial_i \bar{p} + \gamma \bar{p} \, \partial_i \overline{u_i} = \frac{\gamma}{\text{Re Pr}} \partial_i(k \partial_i \bar{T}) + \frac{\gamma - 1}{\text{Re}} \overline{\tau_{ij}} \, \partial_i \overline{u_j} + R_p, \tag{8}$$

where q_{ij} is the subgrid stress (SGS) tensor.

$$q_{ij} = \widetilde{u_i u_j} - \tilde{u}_i \tilde{u}_j. \tag{9}$$

R_m represents the subgrid terms resulting from the nonlinearity of the viscous terms and R_p the subgrid terms in the pressure equation. The subgrid stress q_{ij} is the dominant subgrid term. The term, R_m, and the subgrid term, R_p, in the mean pressure equation can be neglected for the low Mach numbers considered here.

C. Subgrid models

1. Smagorinsky model

The Smagorinsky model[20] is an eddy-viscosity type model given by:

$$q_{ij} - \tfrac{1}{3} q_{ll} \delta_{ij} = -C_S^2 \Delta^2 |\bar{S}| \overline{S_{ij}} \quad \text{with} \quad |\bar{S}|^2 = \tfrac{1}{2} \overline{S_{pq} S_{pq}} \tag{10}$$

and

$$S_{ij} = \frac{1}{2} \left(\frac{\partial u_i}{\partial x_j} + \frac{\partial u_j}{\partial x_i} \right) - \frac{1}{3} \frac{\partial u_l}{\partial x_l} \delta_{ij} \tag{11}$$

is the deviatoric part of the rate of strain tensor. The constant C_s depends on the particular flow and different values have been proposed. Although simple, the Smagorinsky model is known to be excessively dissipative in transitional flows as well as flows with strong coherent structures and to have poor correlation with the exact subgrid stress tensor in *a priori* studies. Here, $C_s = 0.13$ which corresponds to the average value obtained in the dynamic Smagorinsky model LES by Vreman *et al.*[21] of the shear layer.

The gradient of the term, $q_{ll} \delta_{ij}/3$, is absorbed in the pressure gradient for incompressible flows. For the jet studied here, the gradient of $q_{ll} \delta_{ij}/3$ is found to be small in the mean momentum balance and neglected.

2. Mixed model

Another model, the scale-similarity model, which is not based on an eddy-viscosity hypothesis, has been formulated by Bardina *et al.*[22] that, among other advantages, allows backscatter of energy from subgrid scales to resolved scales.

,It is built on the assumption that filtering at different levels results in subgrid stresses with similar structure and is given by

$$q_{ij} = \overline{\overline{u_i} \, \overline{u_j}} - \overline{\overline{u}_i \overline{u}_j}. \tag{12}$$

The correlation of this model with the subgrid stress tensor is known to be much better than in the case of the Smagorinsky model. Although less dissipative than the Smagorinsky model in the transitional zone, it sometimes does not provide enough dissipation in fully turbulent flows for numerical stability. In the mixed model, the scale-similarity model is added to the Smagorinsky model to exploit the advantages of both models,

$$q_{ij} = -C_S^2 \Delta^2 |\overline{S}| \overline{S_{ij}} + \overline{\overline{u}_i \overline{u}_j} - \overline{\overline{u}}_i \overline{\overline{u}}_j. \tag{13}$$

The recent study of Shao et al.[23] shows that there is a physically based reason for the two parts of the mixed model. The scale-similarity part is better suited to account for mean flow effects on the SGS energy transfer and anisotropy, while the Smagorinsky model is appropriate for representing the classical, dissipative energy cascade from the grid scales to the subgrid scale motion.

3. Dynamic eddy-viscosity model

A modification of the Smagorinsky model has been proposed by Germano et al.[24] to correct the excessive dissipation of this model and avoid ad hoc flow-dependent changes to the coefficient. The square of the constant C_s^2 is replaced by a coefficient C_d which is dynamically computed and depends on the local structure of the flow. The Smagorinsky eddy-viscosity formulation is retained:

$$q_{ij} - \tfrac{1}{3}q_{ll}\delta_{ij} = -C_d \Delta^2 |\overline{S}| \overline{S_{ij}}. \tag{14}$$

In order to compute C_d, a test filter, denoted by a hat and corresponding to a filter width larger than that of the LES, is introduced. The consecutive $\hat{\overline{\Delta}}$ application of these two filters defines a filter with a filter width of $\kappa\Delta$. For the top-hat filter, the optimum value $\kappa = \sqrt{5}$, which corresponds to a test filter width of 2Δ, was found in a recent study of the mixing layer.[25] The dynamic constant is calculated with a least squares approach according to:

$$C_d = \frac{\langle M_{ij} L_{ij} \rangle}{\langle M_{ij} M_{ij} \rangle}, \tag{15}$$

$$L_{ij} = \widehat{\overline{u}_i \, \overline{u}_j} - \widehat{\overline{u}}_i \widehat{\overline{u}}_j, \tag{16}$$

$$M_{ij} = -(\kappa\Delta)^2 |\hat{\overline{S}}| \widehat{\overline{S}}_{ij} + \Delta^2 \widehat{|\overline{S}| \overline{S_{ij}}}. \tag{17}$$

To prevent numerical instability caused by negative values of C_d, the numerator and denominator are averaged in the homogeneous directions. The constant C_d is artificially set to zero during the few instances when it is still negative.

4. Dynamic mixed model

The dynamic mixed model is still the sum of the similarity model and the Smagorinsky model but the constant of the Smagorinsky part is dynamically computed. This model takes advantage of the correct dissipation produced by the

dynamic eddy-viscosity part while the similarity part allows other effects such as the backscatter of energy from subgrid scales to resolved scales and anisotropic energy transfers between grid and subgrid scale motion. The mixed SGS model is given by

$$q_{ij} = \overline{\overline{u_i u_j}} - \overline{\overline{u}}_i \overline{\overline{u}}_j - C_d \Delta^2 |\overline{S}| \overline{S_{ij}}. \tag{18}$$

The dynamic model coefficient is obtained by:

$$H_{ij} + C_d M_{ij} = L_{ij}, \tag{19}$$

where M_{ij} and L_{ij} are defined by Eqs. (16)–(17), respectively, and H_{ij} is as follows:

$$H_{ij} = \widehat{\overline{\overline{u}}_i \widehat{\overline{\overline{u}}}_j} - \widehat{\overline{\overline{u}}}_i \widehat{\overline{\overline{u}}}_j - (\widehat{\overline{u}_i \, \overline{u}_j} - \widehat{\overline{\overline{u}}_i \overline{\overline{u}}_j}). \tag{20}$$

The dynamic model coefficient is obtained with the least-squares approach:

$$C_d = \frac{\langle M_{ij}(L_{ij} - H_{ij}) \rangle}{\langle M_{ij} M_{ij} \rangle}. \tag{21}$$

III. NUMERICAL METHOD

The numerical method of the recent DNS by Stanley and Sarkar[18] of the plane jet which is based on their earlier studies[26,27] is used here and summarized below for completeness.

A. Spatial integration method

The spatial derivatives are computed using a nonuniform fourth-order compact scheme based on the uniform scheme of Lele.[28] Nonuniform third-order compact expressions[26] based on those of Carpenter et al.[29] are used on the boundaries. In order to damp the high wave number spurious oscillations created at the boundaries, a fourth-order nonuniform compact filter is applied to the field at each iteration. The parameter α of the filter is optimized in order to keep the influence of the filter as weak as possible and is set equal to 0.4983. The value $\alpha = 0.5$ corresponds to no filtering. The resulting scheme has overall fourth-order spatial accuracy on stretched grids.

B. Time integration

The fourth-order Runge–Kutta scheme of Carpenter et al.[29] is used for the time integration of the convective terms. It is a five-stage scheme for which the fifth stage is added to improve the stability. To save computational time, the viscous terms are advanced using a first-order scheme. This is implemented by advancing the Euler terms using the fourth-order Runge–Kutta scheme and then evaluating and advancing the viscous terms in time using a first-order scheme. Treating the viscous terms in this way is found to have a negligible impact on the solution accuracy because those terms are small compared to the convective terms for the conditions of the jets simulated here. All the simulations have been performed using a constant CFL number of 1.5.

C. Boundary conditions

The principal difficulty in the simulation of unsteady flows in a truncated open computational domain is the formulation of suitable boundary conditions to take into account all the information passing inward and outward across the boundaries while minimizing spurious reflections. Such nonreflecting boundary conditions have been proposed previously, for example, Thompson[30] and Giles.[31]

For the outflow as well as the upper and lower sidewall boundaries, the nonreflecting conditions of Thompson,[30] based on the characteristic equations, are used. These boundary conditions are allowed to switch between inflow and outflow at each point depending on the instantaneous local normal velocity. The corner points are treated as nonreflecting in planes 45 degrees from the adjacent boundaries. At the nonreflecting outflow points an additional pressure correction term, proposed by Rudy and Strikwerda,[32] is used to maintain the pressure near a specified free-stream pressure.

At the inflow boundary, the time variation of the incoming characteristic variables is specified while the the equation for the outgoing characteristic variable is solved using internal biased derivatives. This approach allows the proper specification of the incoming characteristic waves at this boundary. Moreover, to isolate the interior of the domain from the effects of the boundary conditions, a buffer zone based on the approach of Hu[33] is used on the nonreflecting boundaries. The buffer zone is a numerical construct that consists of a stretched grid with additional nodes placed around the computational domain where exponential damping terms are added to the governing equations.

Periodic boundary conditions are used in the z direction.

D. Inflow conditions

The longitudinal mean velocity profile at the inflow is a top-hat profile with smooth edges. A hyperbolic tangent profile is used:

$$U = \frac{U_1 + U_2}{2} + \frac{U_1 - U_2}{2} \tanh\left(\frac{y}{2\theta}\right), \tag{22}$$

where θ is the momentum thickness. U_1 designates the longitudinal velocity in the middle of the jet and U_2 is the co-flow velocity. The co-flow velocity is small, $U_2/\Delta U = 0.1$, so that, for the streamwise distances considered here, the evolution is similar to that of a jet with no co-flow. The mean lateral velocity is initialized as $V = 0$ while the density and the pressure are uniform.

A broadband forcing representative of isotropic turbulence is utilized at the inflow. The three-dimensional energy spectra of the velocity fluctuations at the inflow is

$$E(k) = \frac{k^4}{16} \exp[-2(k/k_0)^2], \tag{23}$$

where the peak frequency k_0 is set to the most unstable mode for the hyperbolic tangent shear layer. The lateral shape, across the jet, is such that the fluctuation intensity peaks in the shear layers on either side of the jet.

IV. LOW REYNOLDS NUMBER SIMULATIONS

A. The jet parameters

The case presented here corresponds to three-dimensional simulations of a ''strong'' jet. The jet is called strong since the co-flow velocity U_2 is weak compared to the jet centerline velocity, resulting in a strong shear layer at the jet edges. The ratio of the velocity between the low- and high-speed streams is 0.09. The ratio of the jet slot width to the inflow momentum thickness, $d/\theta = 20$.

The jet Reynolds number of this simulation is $Re_d = \rho \Delta \overline{U_j} d/\mu = 3000$, where $\Delta \overline{U_j}$ is the velocity difference between the two streams at the inflow and d is the jet slot width. The Reynolds number has been chosen to be the same as those of the direct numerical simulation of Stanley and Sarkar[18] and is sufficiently small to enable an accurate DNS that resolves all relevant spatio-temporal scales on the computational mesh. The Reynolds number based on the initial shear layer momentum thickness is $Re_\theta = 150$.

The Mach number of the high-speed stream is 0.35 and the convective Mach number of the shear layer is $M_c = 0.16$. At such Mach numbers, the physical characteristics of the flow are similar to those of an incompressible flow. The subgrid modeling in LES of this flow can then be regarded as incompressible, which implies that the subgrid stress tensor q_{ij} is the only subgrid term which needs to be modeled.

Broadband inflow conditions obtained by filtering the inflow perturbations in the DNS were used with a maximum fluctuation intensity of $q/\Delta U = 0.1$ in the shear layer.

B. Computational parameters in the DNS

A $205 \times 189 \times 60$ computational grid is utilized in the DNS.[18] The computational domain of interest has the following dimensions: $L_x = 12, L_y = 15$, and $L_z = 4$. All the meshes have been nondimensionalized by the jet slot width d. These dimensions do not include the additional buffer zones at the jet exit and sides. The mesh is uniform in the x direction with $h_x = 0.0666$. In the y direction, it is uniform in the center of the jet from $y = 8$ to $y = 12$ (where $y = 8$ represents the center of the jet) with a grid spacing $h_y = 0.0666$ and then is slightly stretched until the side buffer zones. The mesh is then mirrored across the centerline of the domain. In the spanwise direction, the mesh is also uniform with $h_z = 0.0666$. This mesh is thus almost uniform and homogeneous in all the directions with a grid spacing $h = 0.0666$. This accuracy has been found to be satisfactory and the results compare well with the experimental results.

C. Description of the LES

For the LES, a $61 \times 105 \times 16$ computational grid (Figs. 1–2) has been constructed with a domain size equal to that of the DNS. The mesh has approximately a factor of 22 fewer points than the DNS grid. We have tried to keep the grid as uniform as possible in the LES. In the x direction, the grid is relatively fine between 0 and 1 with $h_x = 0.1$ in order to have adequate numerical resolution of the inflow region. Between $x = 2$ and $x = 12$ the grid is uniform with a grid spacing h_x
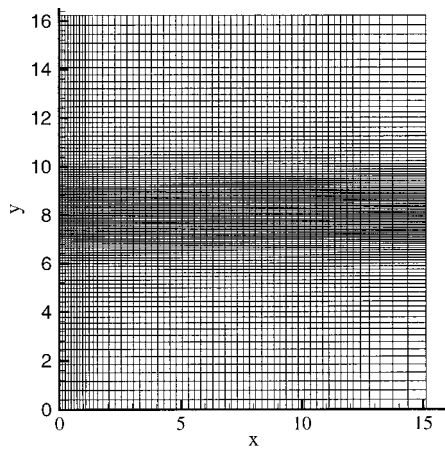
Phys. Fluids, Vol. 11, No. 10, October 1999

Large eddy simulation of a plane jet 3073

FIG. 1. Computational grid on a x-y section. The buffer zone, $12 < x < 15$, at the outflow and $0 < y < 3$, $13 < y < 16$ at the sides is also shown.

$=0.25$ and a short transition zone between $x = 1$ and $x = 2$. In the y direction, the grid is relatively fine between $y = 7$ and $y = 9$ with $h_y = 0.066\,66$ in order to resolve the initial shear layer and then a slight stretching is used until the side buffer zone. In the z-direction the grid is uniform with $h_z = 0.25$.

A computation was attempted on the LES grid without any LES model. This computation was unstable which confirms the necessity of a LES model.

Subsequently, the Smagorinsky, the dynamic Smagorinsky, and the dynamic mixed models are tested. Three filter sizes are also tested: $\Delta = h$, $\Delta = 2h$ and $\Delta = 4h$, where h is the local grid spacing.

For the dynamic mixed model, it is found necessary to introduce a small damping coefficient with magnitude between 0 and 1 that multiplies the similarity part of the model in the initial region $0 < x < 1$. If this damping is not present, the numerical viscosity produced by the Smagorinsky part is not strong enough to stabilize the computation. The similarity part is then fully active downstream of $x = 1$.

D. Deardorff correction

In order to compare the turbulent intensities obtained in the LES with corresponding DNS results we have the choice to either filter the DNS results on the coarse grid as proposed in Vreman *et al.*,[21] or to take into account the energy of the modeled subgrid scales to correct the LES solution for the turbulent intensities. The second solution is preferred because we also want to make comparisons with available experimental results where filtering on the LES grid is not possible. The Deardorff correction[34] is thus applied to the fluctuations of the velocity:

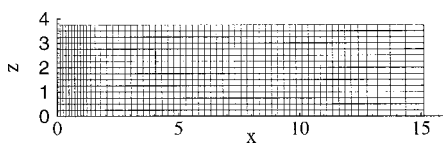$$\text{rms}(u) = \text{rms}(u) + 2/3(\nu_t/C_s\Delta)^2, \quad (24)$$

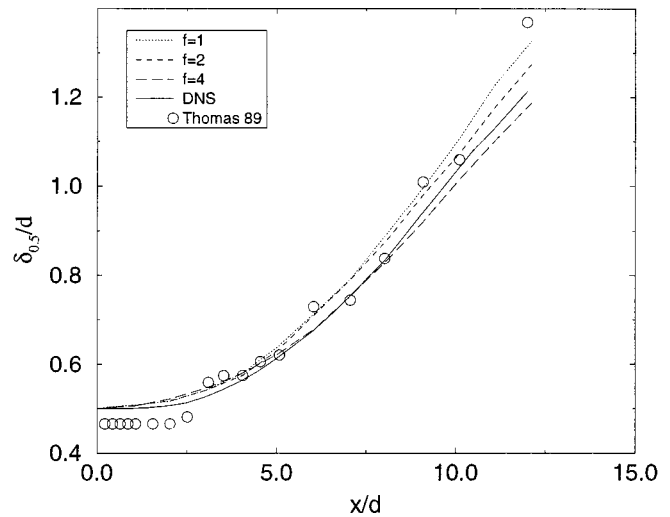FIG. 2. Computational grid on a x-z section.

FIG. 3. Downstream evolution of the jet half-width with different filter sizes for the dynamic Smagorinsky model. The ratio of the filter size to the grid spacing is denoted by f.

$$\text{rms}(v) = \text{rms}(v) + 2/3(\nu_t/C_s\Delta)^2, \quad (25)$$

$$\text{rms}(w) = \text{rms}(w) + 2/3(\nu_t/C_s\Delta)^2, \quad (26)$$

where $C_s = 0.1$. The effect of this correction is to slightly increase the turbulent intensities calculated from LES.

E. Influence of the filter size

Different filter sizes are now tested and compared in order to determine the optimal choice. For the filter size $\Delta = 4h$ only, the spanwise size of the domain is increased in the z-direction because the 16 nodes available in the previous mesh leads to problems during the numerical implementation of the "test" filter in the dynamic procedure. The mesh is kept unchanged in the x and y directions. The dimensions of the new computational domain are $L_x = 12$, $L_y = 15$, and $L_z = 8$, while the number of grid points is $61 \times 105 \times 32$.

The downstream evolution of the jet half-width for the different filter sizes is presented in Fig. 3 for the dynamic Smagorinsky model. When the filter size increases, the growth rate of the jet decreases. The downstream evolution of the centerline fluctuation intensity u_{rms} for the different filter sizes are presented in Fig. 4. The results show significant deterioration when the filter size is chosen to be $\Delta = 4h$ as indicated by substantial underprediction of the turbulence intensity. The next figures present the dynamic constant (Fig. 5) and the subgrid viscosity (Fig. 6) obtained at one section ($x = 10d$) for the different filter sizes with the dynamic Smagorinsky model. It can be seen that, when the filter size increases, the value of the constant slightly decreases. However, the subgrid viscosity increases with filter size because it involves a factor of Δ^2. This increase in subgrid viscosity with filter size is larger than it should be since, as shown in Fig. 3, the jet growth rate is diminished with respect to experimental results for $\Delta = 4h$. Although results are presented here for only the dynamic Smagorinsky model, the preceding remarks are also true for the dynamic mixed model.
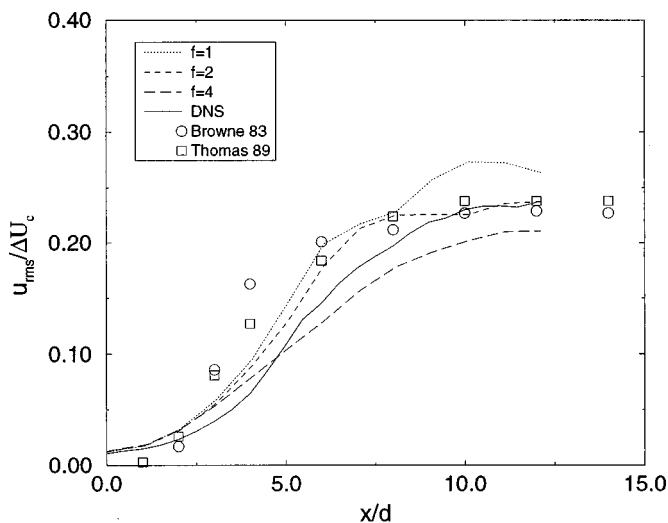
FIG. 4. Downstream evolution of the fluctuation of the longitudinal velocity with different filter sizes for the dynamic Smagorinsky model.
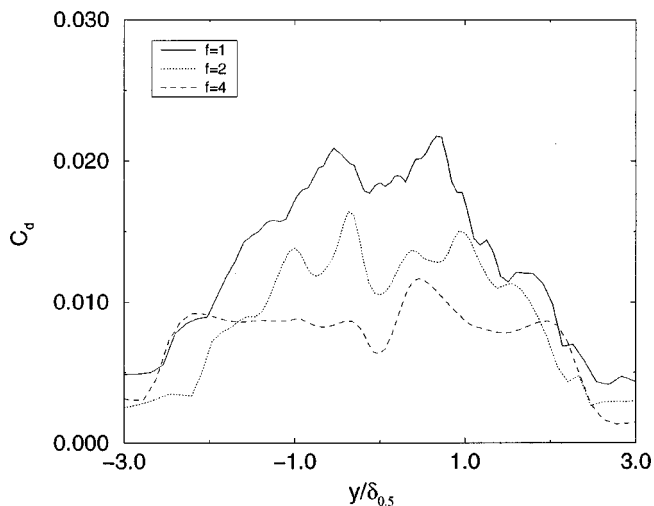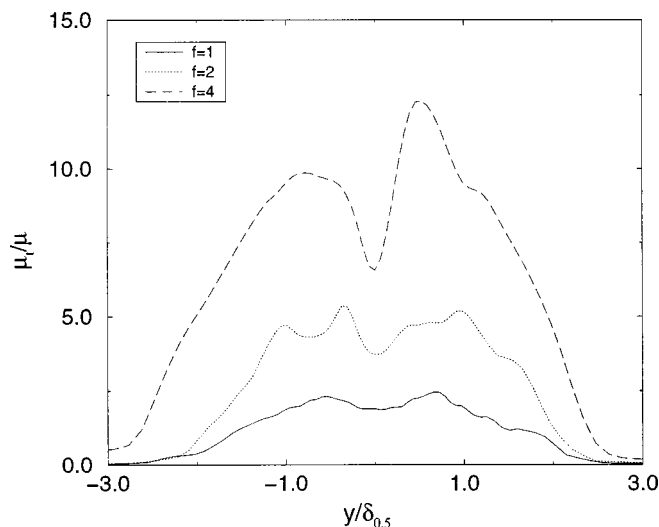

FIG. 6. Comparison of the subgrid viscosity obtained with different filter sizes at the section $x = 10d$ for the dynamic Smagorinsky model.

In the following, only the results produced with a filter size of 2Δ are presented. This size has been chosen because the importance of the subgrid stress in the balance of the momentum equations is higher than for the filter size of Δ without deterioration of the results.

F. Influence of the nonuniformity of the grid

In the x and z directions, the grid is uniform except for a slight stretching between $1 < x < 2$. But in the y direction, to resolve the initial shear layer instabilities, the grid is as fine as the DNS grid in the center of the jet ($7 < y < 9$) and then a slight stretching is used until the buffer zone. The nonuniformity of the grid requires the use of filters with a variable filter width. The use of such filters invalidates the standard derivation of the basic equations for the filtered fields since the filtering operation, in general, does not commute with the operation of differentiation. This problem has been studied

by several authors (Ghosal and Moin,[35] Geurts,[36] Vasilyev et al.[37]) and additional terms in the LES equations or modified filters have been proposed.

In our computation, where the stretching is small, we try to estimate the error due to the noncommutativity of the filtering operation with the differentiation using a formula proposed by Ghosal and Moin:[35]

$$\frac{\overline{d\phi}}{dx} = \frac{d\overline{\phi}}{dx} - \alpha\left(\frac{h'}{h}\right)\frac{d^2\overline{\phi}}{dx^2} + O(kh)^4 \qquad (27)$$

with

$$\alpha = \int_{-\infty}^{+\infty} \xi^2 G(\xi)d\xi, \qquad (28)$$

where G represents the filter function, which is in our case the "top-hat" filter. The error is first computed on the averaged profile of the longitudinal velocity at the section $x = 10d$ and then on an instantaneous profile at the same section. In Fig. 7, the error for the longitudinal velocity at the section $x = 10d$ is presented. The gradients of the averaged and instantaneous longitudinal velocity are also plotted in Fig. 8 to compare with the error term.

As expected, the error is larger on the instantaneous field than on the mean field. In the center of the jet, the error is equal to zero because the mesh is uniform. The region of stretching begins at the border of the jet but the error though nonzero is very small. The local extrema, even in the instantaneous error, are less than 0.2% of the corresponding values of the velocity derivative.

G. Separation between modeling and numerical errors

Large eddy simulations are performed on grids that are just fine enough to resolve the important large-scale flow structures and numerical discretization errors on such grids can have considerable effects on the simulation results. This problem has been recently discussed in the

FIG. 5. Comparison of the dynamic constant obtained with different filter sizes at the section $x = 10d$ for the dynamic Smagorinsky model.
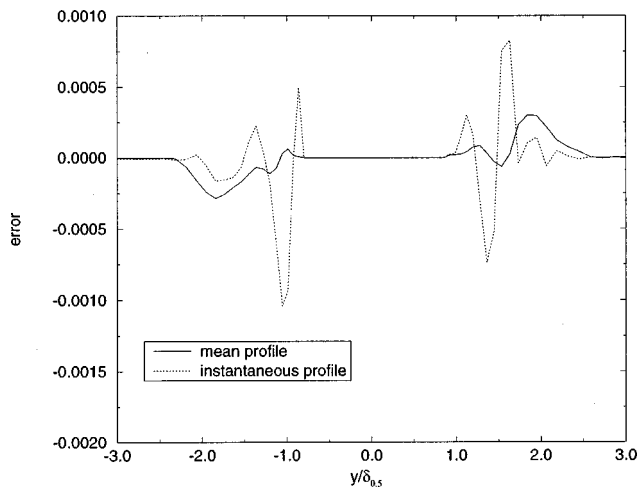
FIG. 7. Comparison of the commutativity error in dU/dy on the mean and instantaneous longitudinal velocity profile at the section $x=10d$ for the dynamic Smagorinsky model.
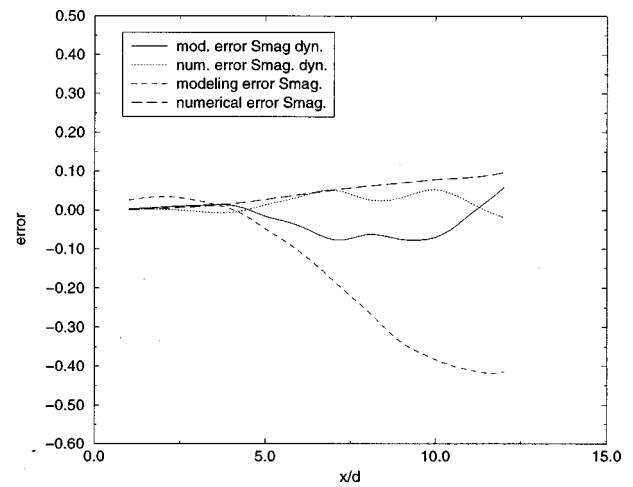

FIG. 9. Comparison of the numerical and the modeling error obtained on the evolution of the jet half-width with the dynamic Smagorinsky and the Smagorinsky model.

literature—Vreman,[38] Salvetti and Beaux,[39] Kravchenko and Moin.[40] The difference between LES and DNS is referred to as the total error. It is the sum of two terms: a modeling error arising from the subgrid model and the discretization error caused by the numerical method. A method to separate those two errors has been proposed by Vreman[38] based on the expectation that the discretization error in the LES decreases when the resolution is increased with the filter width kept constant.

A new LES is then performed on a finer grid keeping the same filter width. The grid step has been divided by two in the x and z directions. In the y direction, the same grid step is kept because in the center of the jet, it is as fine as the DNS grid.

The difference between those two LES represents the effects of the numerical error:

$$\text{err}_{\text{num}} = \text{err}_{\text{LES}} - \text{err}_{\text{fine grid LES}} \qquad (29)$$
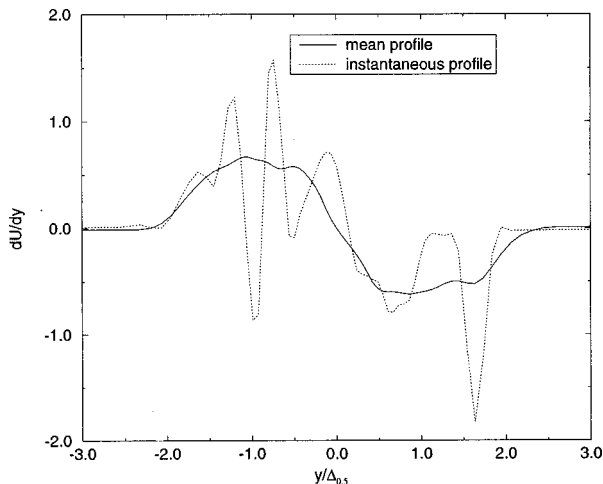
and the differences between the fine grid LES and the DNS represents the modeling error:

$$\text{err}_{\text{mod}} = \text{err}_{\text{fine grid LES}} - \text{err}_{\text{DNS}}. \qquad (30)$$

Figure 9 shows the effects of those two errors on the evolution of the jet half width. The discretization error is generally smaller than the modeling error. The modeling error associated with the Smagorinsky model is much larger than that produced by the dynamic Smagorinsky model indicating the superiority of the dynamic procedure. The discretization error and the modeling error have opposite signs which implies that the discretization error assists the subgrid model and that the total error is then smaller than the modeling error. This observation suggests that, for this example, grid refinement may not necessarily give rise to smaller total errors. Nevertheless, both modeling and discretization errors are small with the dynamic Smagorinsky model. Interestingly, Vreman[38] also observed opposite signs of numerical and modeling errors in the temporally-evolving mixing layer.

H. Computational results

1. Evolution of the mean flow

The profiles of the longitudinal velocity obtained with the dynamic Smagorinsky model (Fig. 10) and with the dynamic mixed model (Fig. 11) are first presented. Similarity coordinates are used with the transverse y direction normalized by the local jet half-width $\delta_{0.5}$ and the jet velocity difference with respect to the small co-flow normalized by its value at the centerline, ΔU_c.

The longitudinal mean velocity profile at the inflow is flat and then, for $x > 6$, develops rapidly to self-preserving profiles. We can see that for $x=2$ the self-preserving profiles are not yet established and that for $x > 8$ the agreement with the experimental results is good for both models.

Similarity profiles of the transverse velocity (not shown here) for the dynamic Smagorinsky model and for the dy-
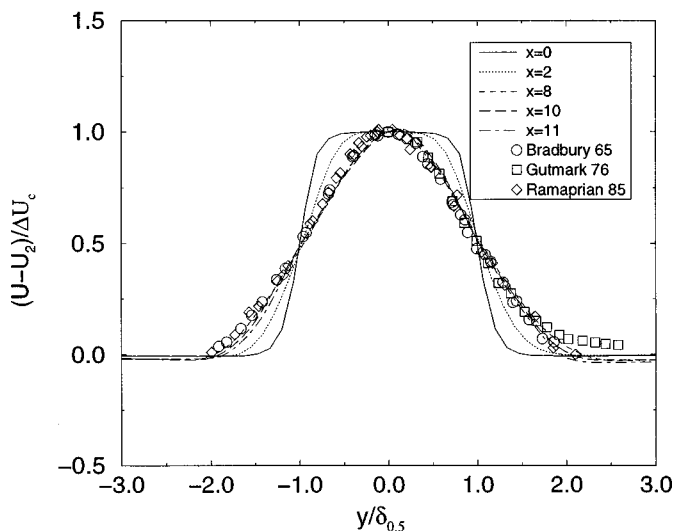

FIG. 8. Comparison of the derivative of the mean and instantaneous longitudinal velocity profile at the section $x=10d$ for the dynamic Smagorinsky model.
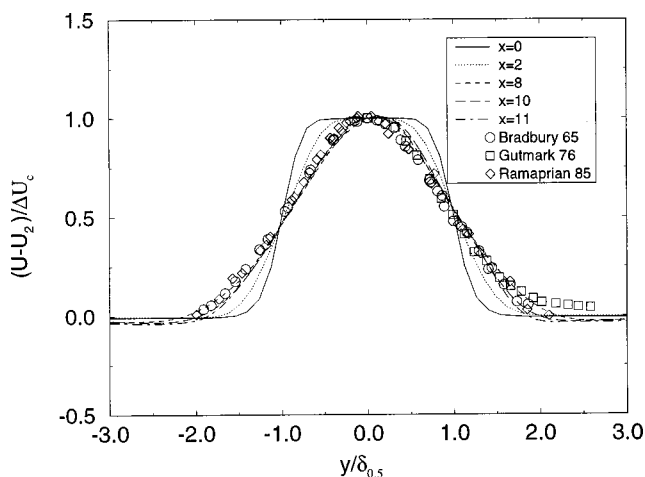
FIG. 10. Dynamic Smagorinsky model: Profiles of the longitudinal velocity at different streamwise locations.

FIG. 12. Downstream evolution of the jet half-width.

namic mixed model are compared with experimental results. The overall agreement with the experimental data is also good.

The downstream evolution of the jet half-width (Fig. 12) and the centerline velocity excess (Fig. 13) are now presented together with the DNS results. The experimental data from Thomas and Chu[5] for a jet with $Re_d = 8300$ and from Browne *et al.*[6] for a jet with $Re_d = 7620$ are also plotted. The excessive dissipation of the standard Smagorinsky model is confirmed and the evolution of the jet half-width and centerline velocity excess are *severely* unpredicted by this model. The two other models both give reasonable results compared with the DNS and experimental results. From the poor prediction of the Smagorinsky model, it is clear that the dynamic approach is required when it is applied to the jet.

When self-similar, the planar jet grows linearly, $\delta_{0.5} \propto x$, while the jet velocity excess $\Delta U_c = U_c - U_2$ decreases as $\Delta U_c \propto x^{-1/2}$. Note that the jet velocity $U_j \gg U_2$, the coflow velocity, so that jetlike behavior is expected without the

wakelike evolution expected for large coflow velocities. Figure 12 shows the evolution of the jet half-width while Fig. 13 shows the evolution of the inverse square of the jet velocity excess; both should show linear evolution if self-similar conditions are achieved. The self-similar behavior of the jet half-width can be fitted to $\delta_{0.5} = K_1 d(x/d + K_2)$.

The DNS evolution in the region $7 < x/h < 12$ is well-described by a linear curve[18] with $K_1 = 0.094$ and $K_2 = 0.904$. The dynamic Smagorinsky model gives $K_1 = 0.094$ and $K_2 = 1.38$ while the dynamic mixed model gives $K_1 = 0.106$ and $K_2 = 0.4$. The LES and DNS results are consistent with experimental data where the growth rate $d\delta_{0.5}/dx = K_1$ is found to vary between 0.1 and 0.11. The jet velocity in the self-similar region can be described as, $\Delta U_j^2 = C_1 \Delta U_c^2 (x/d + C_2)$, where $\Delta U_c(x)$ is the jet velocity excess that decreases with x while ΔU_j is the constant inflow jet velocity excess. The DNS results give $C_1 = 0.208$ and $C_2 = -0.577$ while the LES results give $C_1 = 0.19$ and $C_2 = 0.89$ with the dynamic Smagorinsky model, while $C_1 = 0.22$ and $C_2 = 0.18$ with the dynamic mixed model.
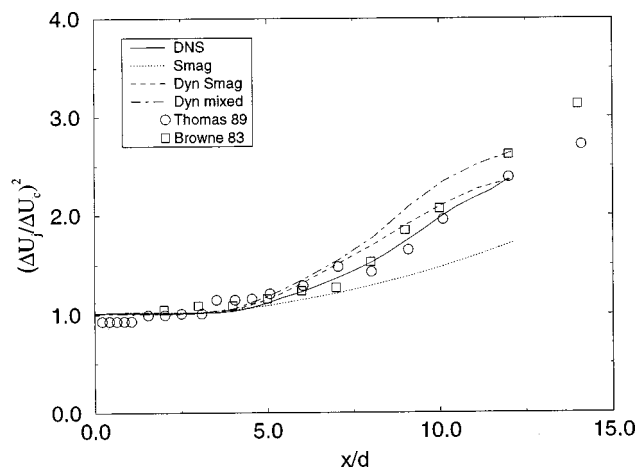

FIG. 11. Dynamic mixed model: Profiles of the longitudinal velocity at different streamwise locations.

FIG. 13. Downstream evolution of the centerline velocity excess.
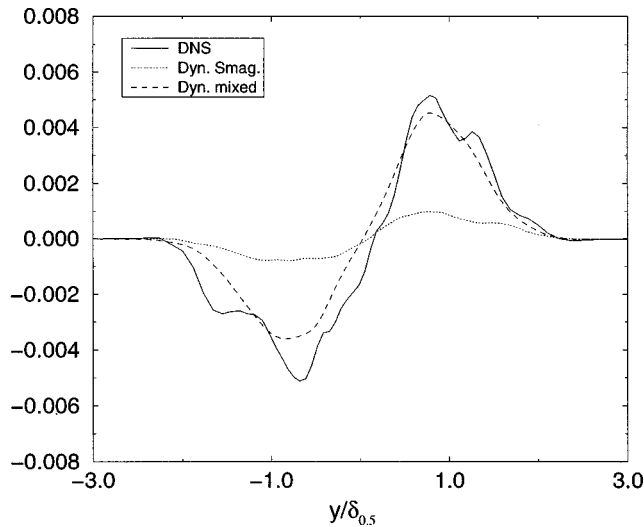
FIG. 14. Profile of the subgrid shear stress $\langle q_{xy} \rangle$.

FIG. 16. Dynamic Smagorinsky model: balance of the streamwise momentum equation at the section, $x = 10d$.

2. Comparison of the subgrid stress tensor

A few instantaneous DNS fields have been filtered on the LES grid, averaged in the spanwise direction, and then ensemble averaged to get an estimate of the Reynolds average $\langle q_{ij} \rangle$ of the subgrid stress tensor defined by Eq. (11). The most important component is the subgrid shear stress, $\langle q_{xy} \rangle$ (obtained by z direction averaging and time averaging), which is compared with the DNS estimate in Fig. 14. The components $\langle q_{xz} \rangle$ and $\langle q_{yz} \rangle$ are negligible.

The dynamic mixed model compares much better with the DNS results than the dynamic Smagorinsky model. The Smagorinsky model is known to have a lower correlation level with the subgrid stress tensor than the similarity model and this finding is confirmed by the present results. The dynamic mixed model predictions of the diagonal components $\langle q_{xx} \rangle, \langle q_{yy} \rangle, \langle q_{zz} \rangle$ (not shown here) are also in good agreement with the DNS results.

The $\langle q_{xy} \rangle$ component of the Reynolds stress is decomposed into its Smagorinsky part and its Bardina part for the
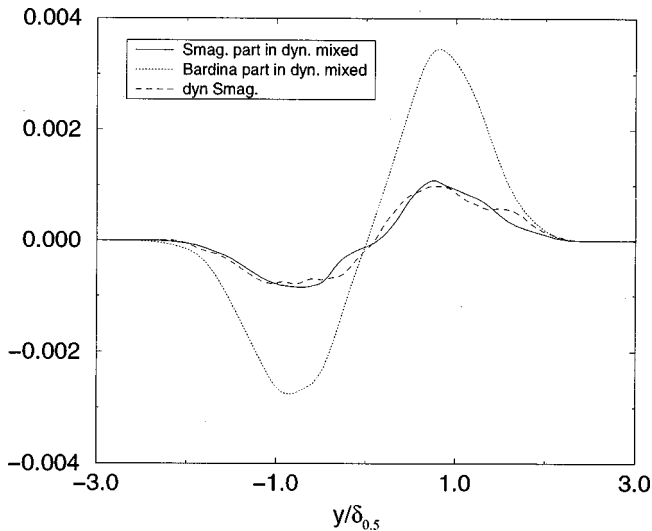

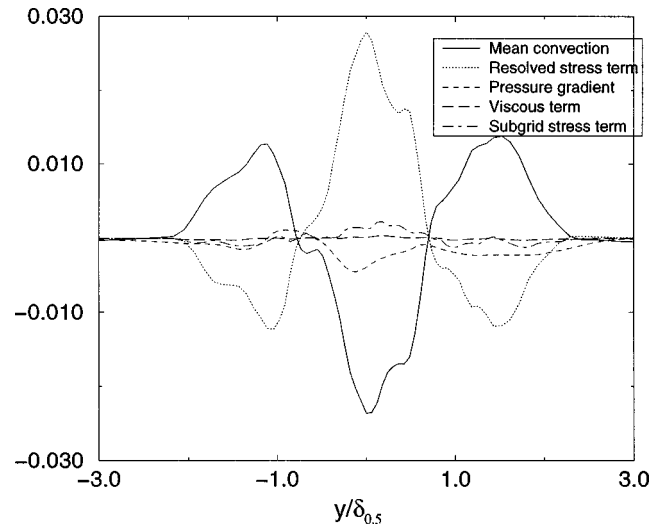FIG. 15. Decomposition of the subgrid shear stress for the mixed model.

dynamic mixed model (Fig. 15). It can be seen that the contribution of the Bardina part is much larger than that of the Smagorinsky part. Also, the Smagorinsky part in the mixed model is similar in magnitude to the dynamic Smagorinsky model.

3. Balance of the momentum equation

To see the importance of the subgrid scale term compared to the other terms, the balance of the momentum equation is presented for the dynamic Smagorinsky model and for the dynamic mixed model.

The filtered momentum equation, Eq. (7), can be Reynolds averaged by averaging in the z-direction and time in the jet so that:

$$\partial_j(\langle \bar{\rho} \rangle \langle \widetilde{u_i} \rangle \langle \widetilde{u_j} \rangle) + \partial_j \langle R_{ij} \rangle + \partial_i \langle \bar{p} \rangle - \frac{1}{Re} \partial_j \langle \overline{\tau_{ij}} \rangle + \partial_j \langle \overline{q_{ij}} \rangle = 0,$$

(31)

where $\langle . \rangle$ denotes Reynolds averaging. The terms on the left hand side represent mean convection, the resolved turbulent stress, the pressure gradient, the viscous stress, and the subgrid stress, respectively. Note that the resolved stress $\langle R_{ij} \rangle = \bar{\rho} \langle \widetilde{u_i'} \widetilde{u_j'} \rangle$ represents the stress associated with the turbulent part of the resolved velocity field while $\langle \overline{q_{ij}} \rangle$ represents the SGS stress associated with the unresolved, modeled part of the fluctuations. The contribution of these terms to the balance of mean streamwise momentum, $\langle \bar{\rho} \rangle \langle \widetilde{u_1} \rangle$, is shown in Figs. 16 and 17. The dominant balance is between mean convection and the transverse gradient of the resolved Reynolds shear stress $\partial_2 \langle R_{12} \rangle$.

The contribution of the subgrid term is much larger in the case of the dynamic mixed model than in the case of the dynamic Smagorinsky model and increases with the filter size. However, the sum of the resolved stress term and the subgrid stress term is approximately *the same* (Fig. 18) for the two models which explains why the LES predictions of
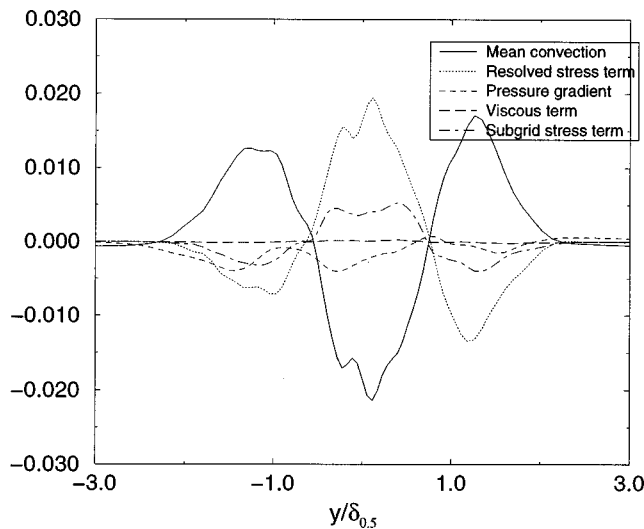
FIG. 17. Dynamic mixed model: balance of the streamwise momentum equation at the section, $x = 10d$.

the mean flow evolution in Figs. 12–13 are similar despite the much better agreement of the mixed model subgrid stress with DNS. Thus, even though the subgrid shear stress in the dynamic Smagorinsky model is far too small relative to the exact value (see Fig. 14), the large resolved stress compensates for the small subgrid term in computations with the dynamic Smagorinsky model.

4. Comparison of the turbulence intensities

The downstream evolution of the longitudinal centerline fluctuation intensities is presented in Fig. 19. The experimental results of Browne *et al.*[6] and Thomas and Chu[5] are also shown. The fluctuating quantities, consistent with experimental studies, develop much slower toward self-preserving profiles than the mean flow. The streamwise rms value increases slowly before $x = 2.5d$ and then increases rapidly to reach the similarity values after $x = 10d$. The excessive dis-
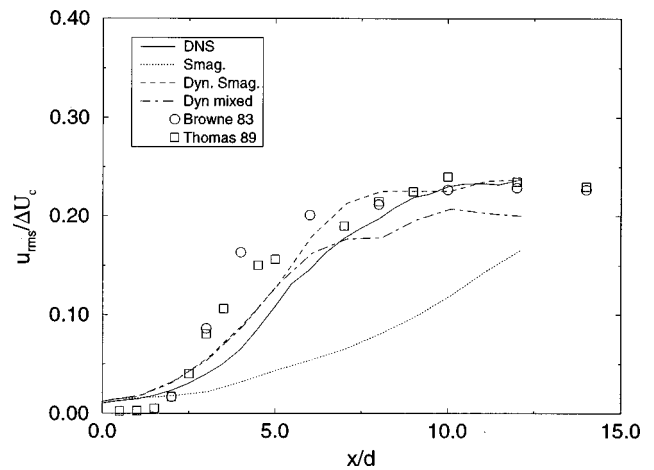

FIG. 19. Downstream evolution of the fluctuation of the longitudinal velocity: comparison between the different models.

sipation of the Smagorinsky model is again shown by the unrealistically small values of the streamwise turbulence intensity. This model will not be discussed further in the following plots. The two other models give the same results until $x = 5d$, then the dynamic Smagorinsky model predicts higher values.

The fluctuation intensity profiles u_{rms} (Fig. 20) are compared with experimental data and DNS. The section $x = 11d$ is chosen because it is the region where self-similarity in the fluctuating quantities begins and is far from the outflow boundary. The overall agreement with the DNS and the experimental results is good. The dynamic Smagorinsky model prediction is perhaps slightly closer to the DNS prediction.

5. Key properties of the SGS models

The downstream evolution of the dynamic constant (Fig. 21) and the subgrid dissipation (Fig. 22) are first presented for the dynamic Smagorinsky model. The dynamic constant
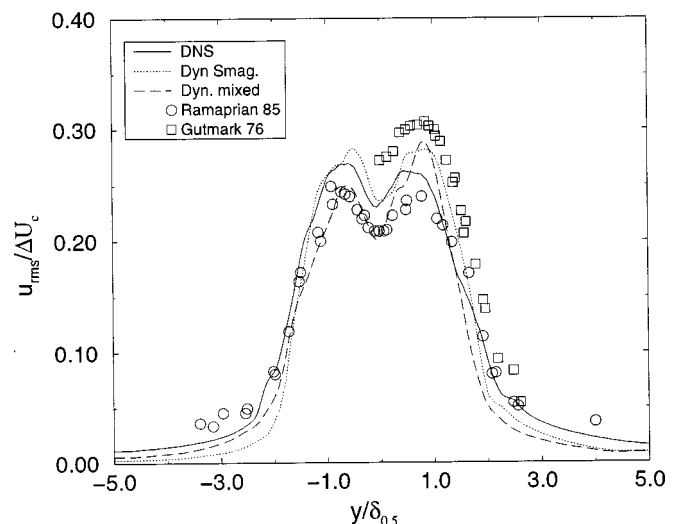

FIG. 18. Comparison of the sum of the resolved stress term and the subgrid stress term for the dynamic Smagorinsky model and the dynamic mixed model at the section $x = 10d$.

FIG. 20. Comparison of the streamwise turbulence intensity obtained with the different models at the section $x = 11d$.
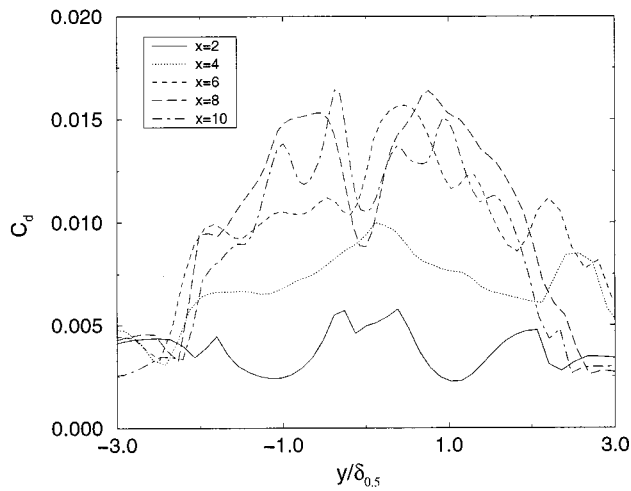
FIG. 21. Dynamic Smagorinsky model: downstream evolution of the dynamic constant.

FIG. 23. Comparison of the dynamic constant obtained with the different models at the section $x = 10d$.

is very small in the shear layer near the inflow, increases rapidly, and after $x = 6$ does not vary much with streamwise distance. The evolution of the subgrid dissipation is similar. It is very small near the inflow due to the small value of the constant and, after an initial transient, varies gradually in the streamwise direction. In the transverse direction, the Smagorinsky coefficient and subgrid dissipation increase from the centerline value, reach a peak, and then decay in the freestream. These remarks on the evolution of the dynamic constant and the SGS dissipation are true for both dynamic models.

The dynamic constant (Fig. 23), the subgrid dissipation (Fig. 24), and the subgrid viscosity (Fig. 25) obtained for the different models at one section ($x = 10d$) are compared. The dynamic constant levels are similar between the dynamic Smagorinsky model and the dynamic mixed model with the same filter size. The level of the Smagorinsky constant $C_d = C_s^2 = 0.017$ is also plotted. It is higher than the constant predicted with the dynamic model with a filter size of Δ
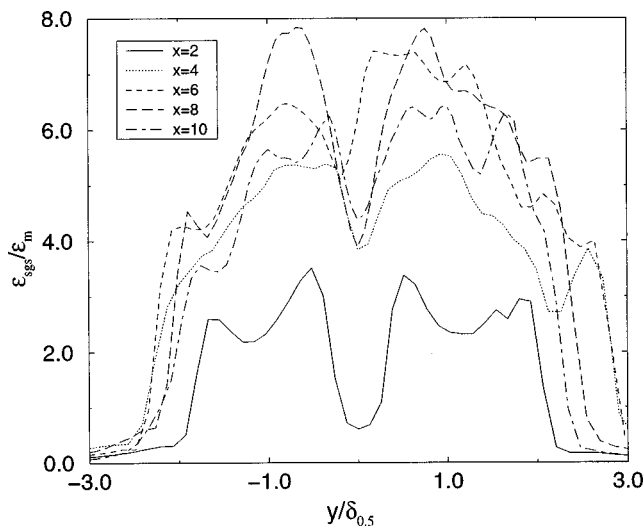
$= 2h$. However, $C_d = C_s^2 = 0.017$ is smaller than the values (not shown here) obtained with the dynamic models and a filter size of $\Delta = h$. The baseline Smagorinsky model has no mechanism to adjust the constant level to the filter size. Moreover, the magnitude of the eddy-viscosity coefficient predicted by the dynamic model near the inflow is much smaller than its value in the fully developed region.

The subgrid dissipation is higher for the dynamic mixed model due to the contribution of the scale-similarity part. The eddy-viscosity contribution is similar for both the dynamic mixed and dynamic Smagorinsky models. For the dynamic mixed model, the two parts of the subgrid dissipation, the Smagorinsky part and the similarity part, are of the same order.

Concerning the subgrid viscosity, the difference between the dynamic Smagorinsky results and the dynamic mixed results is very small which is a consequence of the same level of the constant. The subgrid viscosity produced by the
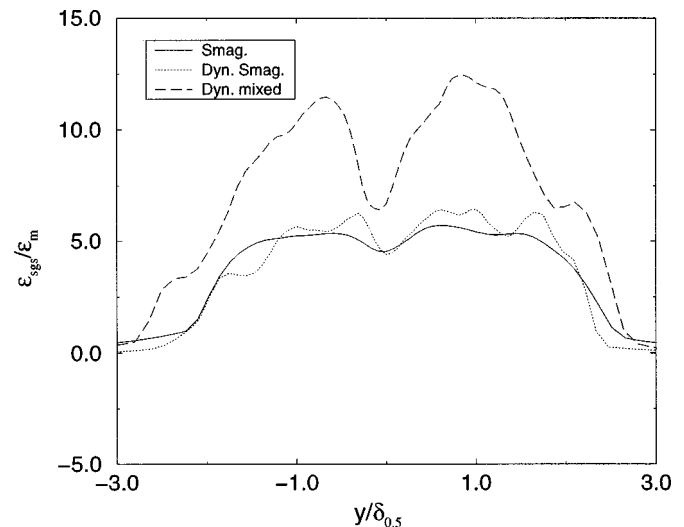

FIG. 22. Dynamic Smagorinsky model: downstream evolution of the subgrid dissipation.

FIG. 24. Comparison of the subgrid dissipation obtained with the different models at the section $x = 10d$.
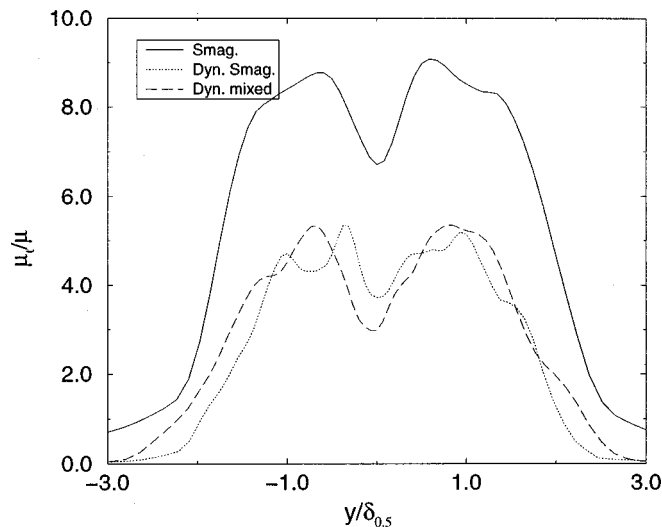
FIG. 25. Comparison of the subgrid viscosity obtained with the different models at the section $x = 10d$.

Smagorinsky model without the dynamic procedure is much higher.

6. Temporal auto-spectrum

The auto-spectrum in time of the centerline longitudinal velocity fluctuation is shown in Fig. 26 for the dynamic mixed model. The spectrum develops rapidly from its initial form at $x = 2d$. Further downstream, the spectral shape for large frequencies ($f \delta_{0.5} / \Delta U > 0.3$) appear to collapse well while significant differences remain at lower frequencies. Large-scale coherent structures have been observed in experiments at the Strouhal number $St = f \delta_{0.5} / \Delta U = 0.11$. Although there is significant energy at $St = 0.11$ as shown in Fig. 26, a dominant discrete peak is not observed for the turbulent jet simulated here.

7. Isocontours of vorticity

Instantaneous isocontours of spanwise vorticity are now presented in an xy-plane. The contours of the z-component of vorticity obtained by the dynamic Smagorinsky model (Fig.
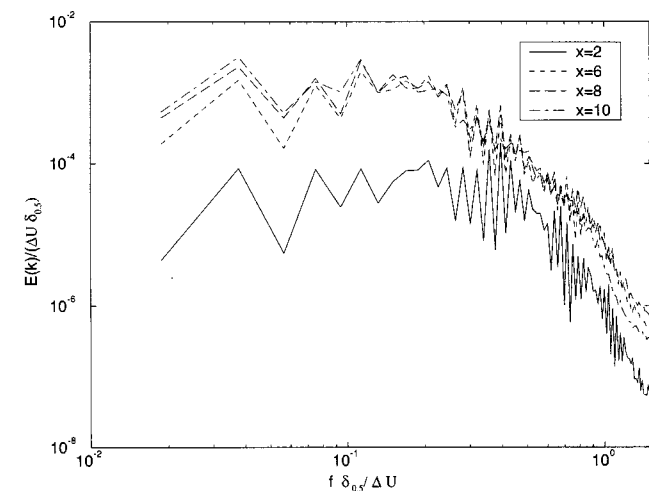

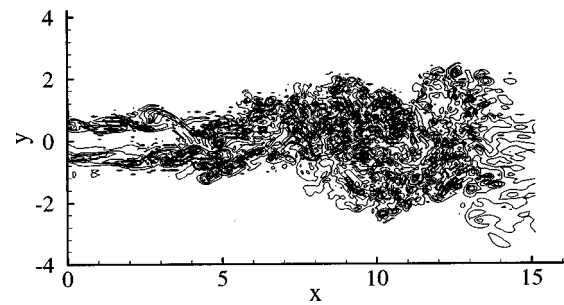FIG. 26. Dynamic mixed model—evolution of the time spectrum.

FIG. 27. DNS: contours of the z-component of vorticity on a xy-plane. Results from DNS of Stanley and Sarkar (Ref. 18).

28) and the dynamic mixed model (Fig. 29) are presented and compared with the DNS contours (Fig. 27).

For $x < 5d$ the largest Kelvin–Helmholtz rollers of the two mixing layers at the jet edge appear clearly. These mixing layers develop symmetrically and start breaking down into small scales. After $x = 5d$ the two mixing layers merge, a rapid breakdown of the large structures with a growth of the small structures occurs, and the development of the jet becomes asymmetric. The instantaneous large-scale structures of the jet in the LES compares well with the DNS results. Although the LES qualitatively captures the large-scale structures in the DNS, the small-scale features are absent as would be expected.

V. HIGH REYNOLDS NUMBER COMPUTATIONS

A higher Reynolds number jet is now considered. The Reynolds number is set to $Re_d = 30\,000$ corresponding to the experiment of Gutmark and Wygnanski.[7] A strong influence of the Reynolds number is, however, not observed in experimental data for jets developing from turbulent initial conditions.

The length of the computational domain is also increased so as to capture a larger extent of the jet development. Consequently, the height of the computational domain is also increased to account for the expansion of the jet. The dimension of the new domain are: $L_x = 20, L_y = 32$, and $L_z = 6$. These dimensions do not include the buffer zone. For $y < 12d$, we have tried to keep the grid as close to the preceding grid as possible. The new grid has $93 \times 137 \times 16$ points. No DNS results are available because the Reynolds number is too high to resolve all scales of motion. The LES results are now compared with experimental results.
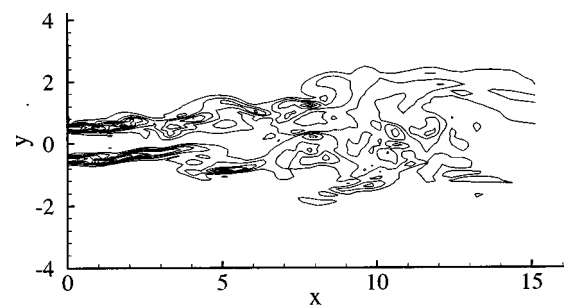

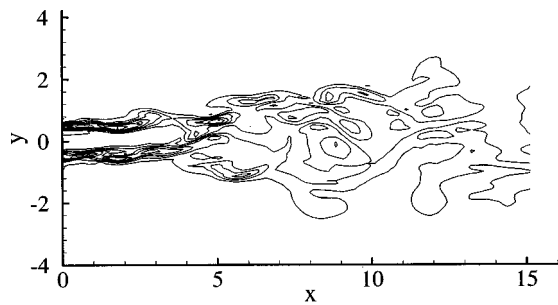FIG. 28. Dynamic Smagorinsky model: contours of the z-component of vorticity on an xy-plane.

FIG. 29. Dynamic mixed model: contours of the z-component of vorticity on an xy-plane.

FIG. 31. Comparison of the streamwise turbulence intensity obtained the the different models at the sections $x=19d$: jet with $Re_d=30\,000$.

A. Evolution of the mean flow

The downstream evolution of the jet half-width is first presented for the two models together with experimental results (Fig. 30). For $x<12$, the results are similar to those obtained on the preceding grid for the lower Reynolds number. Note that both the low and high Reynolds number simulations jets have turbulent inflow conditions. The coefficients of the linear curve fit to the jet half-width evolution are $K_1=0.094$ and $K_2=1.66$ for the dynamic Smagorinsky model and $K_1=0.091$, $K_2=1.97$ for the dynamic mixed model. The values of the growth rate K_1 are in good agreement with the values obtained in experiments.

B. Comparison of the turbulence intensities

Profiles of streamwise fluctuation intensity, v_{rms}, at a single section ($x=19h$) are plotted in Fig. 31 and compared with the experimental data of Gutmark and Wygnanski[7] and Ramaprian and Chandrasekhara.[3] The agreement with experimental results is good although the difference between the two models is larger at this section. Similar to the lower Reynolds number computations, the maximum of the fluctuation intensity for the dynamic mixed model is somewhat smaller than the dynamic Smagorinsky model. Profiles at various streamwise locations are then presented (Fig. 32) and
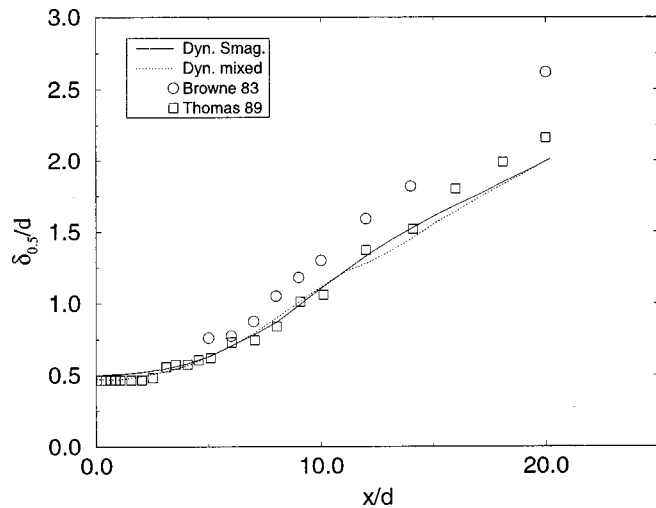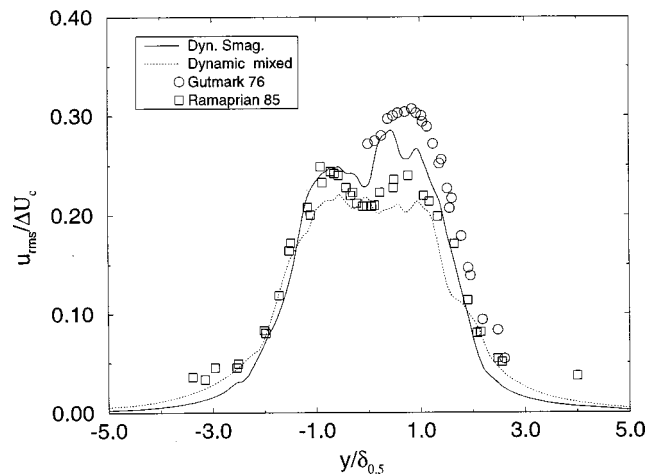
it can be seen that, after $x\simeq14d$, the profiles approach self-similarity.

C. Key properties of the SGS model

The dynamic constant (Fig. 33) and the subgrid dissipation (Fig. 34) obtained by the two models are plotted and compared at the section ($x=19d$). The dynamic constant obtained with the two models remains the same and is slightly smaller than the constant at the section $x=8d$ in the simulation of the lower Reynolds number jet.

The subgrid dissipation compared to the molecular dissipation is much higher here than for the low Reynolds number case due to the decrease in the molecular dissipation. The dissipation produced by the dynamic mixed model remains higher than the Smagorinsky model due to the scale-similarity part.

VI. CONCLUSIONS

In this paper *a posteriori* tests of LES in the case of a spatially developing jet have been presented. The computa-

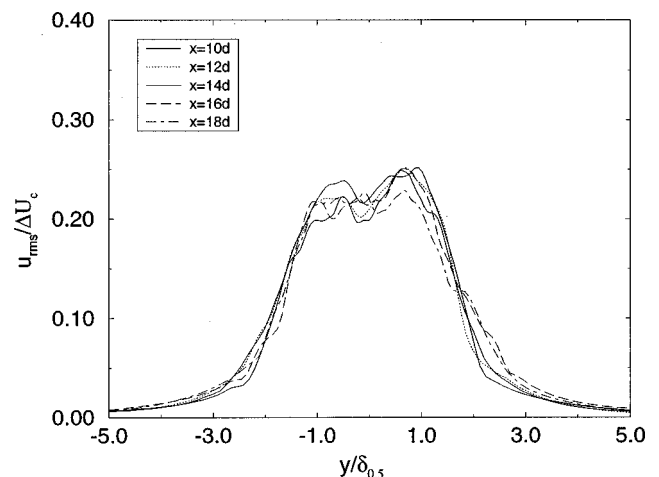FIG. 30. Downstream evolution of the jet half-width: high Reynolds number jet with $Re_d=30\,000$.

FIG. 32. Profiles of the streamwise turbulence intensity obtained with the dynamic mixed model at different sections: jet with $Re_h=30\,000$.
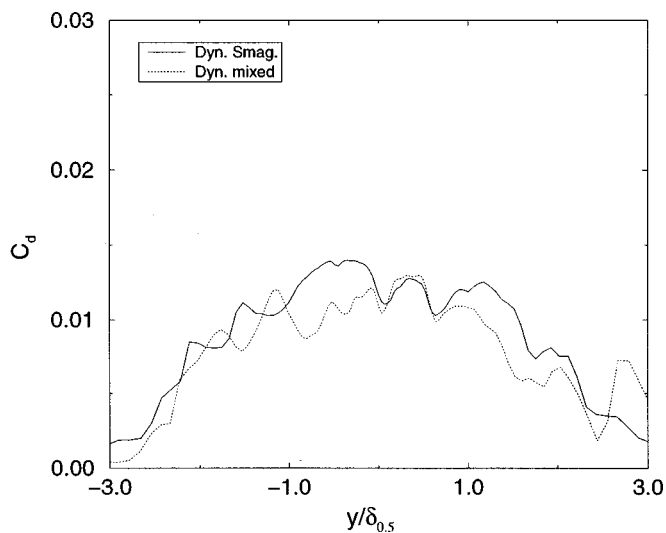
FIG. 33. Comparison of the dynamic constant obtained with the different models at the section $x=19d$: jet with $Re_d=30\,000$.

tion starts from the initial region of the jet with broadband inflow disturbances and captures its natural development from a turbulent inflow. Three different subgrid stress models are compared: the standard Smagorinsky model, the dynamic Smagorinsky model, and the dynamic mixed model. Different filter sizes corresponding to $\Delta=h$, $\Delta=2h$, and $\Delta=4h$ are also tested. A series of simulations at a low Reynolds number $Re_d=3000$ is performed to enable comparisons with DNS data. Then the Reynolds number is increased and simulations are performed at a high Reynolds number, $Re_d=30\,000$, more typical of engineering applications.

The quality of the LES model is determined by comparison with previous DNS[18] and experiments.[2–7] Computations performed on the LES grid without the LES model show numerical instability which confirms the necessity of a subgrid stress model. Comparison of different filter sizes shows that the filter size $\Delta=h$ and $\Delta=2h$ give similar good results, while, with the filter size $\Delta=4h$, the results are poorer. Subsequent results are presented and compared with a filter size
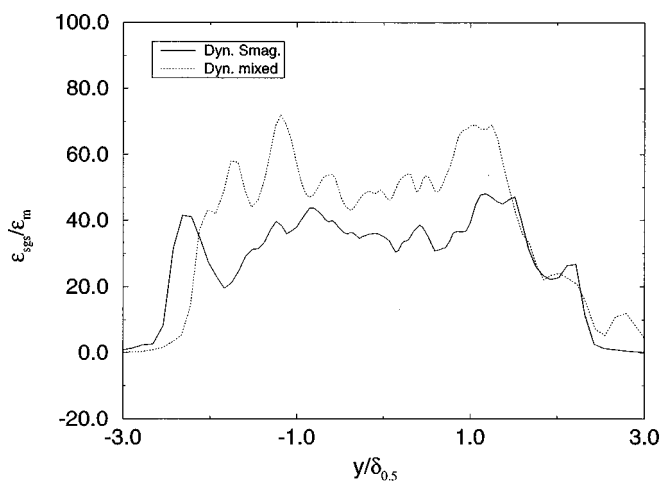
$\Delta=2h$. Moreover, this filter size has been suggested by Vreman et al.[21] in the case of high-order finite difference simulations.

Predictions of the three models (standard Smagorinsky, dynamic Smagorinsky, and dynamic mixed) are compared. The standard Smagorinsky model is used with a coefficient $C_s=0.13$ which, although lower than the value for isotropic turbulence, has been found to be better suited to shear flows. Even so, it is found that the subgrid dissipation given by the standard Smagorinsky model during the initial evolution of the jet is excessively high resulting in substantial underprediction of the jet width. It is clear that, when the Smagorinsky model is used, a dynamic procedure is required to predict the growth rate of the jet as well as its turbulence intensities. Concerning the overall prediction of the mean field and the Reynolds stress, the two other models are both in good agreement with experimental and DNS results. The evolution of the jet growth rate and the centerline velocity excess compares well and self-similarity profiles are obtained. The growth of the turbulence intensities is also relatively well predicted. The evolution and comparison of some quantities such as the dynamic constant, the subgrid viscosity, and the subgrid dissipation are also presented. There is substantial variation of the dynamic Smagorinsky coefficient across the jet and during the initial streamwise evolution. The subgrid dissipation associated with the dynamic mixed model is larger than that given by the dynamic Smagorinsky model.

From previous a priori tests, the dynamic mixed model is known to provide a much better representation of the subgrid stress tensor and that is confirmed by our a posteriori simulations. On the other hand, the dynamic Smagorinsky model severely underpredicts the magnitude of the subgrid shear stress but, surprisingly, provides satisfactory overall results concerning the mean flow. It is of interest to determine why LES with the dynamic Smagorinsky model is equally successful as the dynamic mixed model despite the poor prediction of the subgrid stress. After examination of the mean momentum balance, it is found that the sum of the resolved and subgrid shear stress is similar with both models, thus explaining their similar performance.

The second series of LES considers a jet at a much higher Reynolds number, $Re_d=30\,000$, in a larger computational domain. No DNS results are available for comparison since the Reynolds number is too high to accurately resolve all the scales, but experimental results are available. Compared to the lower Reynolds number, $Re_d=3000$ computations, no strong differences in the results appear which is consistent with the experimental data in jets starting with turbulent inflow conditions. The downstream evolution of the mean flow compares well with experimental data and similarity profiles are obtained for the intensities of velocity fluctuations. The subgrid dissipation compared to the molecular dissipation is much higher than that in the low Reynolds number case.

ACKNOWLEDGMENTS

FIG. 34. Comparison of the subgrid dissipation obtained with the different models at the section $x=19d$: jet with $Re=30\,000$.

[1] R. A. Antonia, L. W. B. Browne, S. Rajagopalan, and A. J. Chambers, ''On the organized motion of a turbulent plane jet,'' J. Fluid Mech. **134**, 49 (1983).

[2] F. O. Thomas and K. M. K. Prakash, ''An experimental investigation of the natural transition of an untuned planar jet,'' Phys. Fluids A **3**, 90 (1991).

[3] B. R. Ramaprian and M. S. Chandrasekhara, ''LDA measurements in plane turbulent jets,'' ASME Fluids Eng. **107**, 264 (1985).

[4] L. J. S. Bradbury, ''The structure of a self-preserving turbulent plane jet,'' J. Fluid Mech. **23**, 31 (1965).

[5] F. O. Thomas and H. C. Chu, ''An experimental investigation of the transition of a planar jet: Subharmonic suppression and upstream feedback,'' Phys. Fluids A **1**, 1566 (1989).

[6] L. W. B. Browne, R. A. Antonia, S. Rajagopalan, and A. J. Chambers, ''Interaction region of a two-dimensional turbulent plane jet in still air,'' in *Structure of Complex Turbulent Shear Flow*, edited by R. Dumas and L. Fulachier IUTAM Symp. Marseille (Springer, New York, 1983), pp. 411–419.

[7] E. Gutmark and I. Wygnanski, ''The planar turbulent jet,'' J. Fluid Mech. **73**, 465 (1976).

[8] R. A. Antonia, A. J. Chambers, D. Britz, and L. W. B. Browne, ''Organized structures in a turbulent plane jet: Topology and contribution to momentum and heat transport,'' J. Fluid Mech. **172**, 211 (1986).

[9] F. O. Thomas and V. W. Goldschmidt, ''Structural characteristics of a developing turbulent plane jet,'' J. Fluid Mech. **163**, 227 (1986).

[10] F. O. Thomas and V. W. Goldschmidt, ''Acoustically induced enhancement of widening and fluctuation intensity in a two-dimensional turbulent jet,'' ASME J. Fluids Eng. **108**, 331 (1986).

[11] I. Namer and M. V. Otugen, ''Velocity measurements in a plane turbulent air jet at moderate Reynolds numbers,'' Exp. Fluids **6**, 387 (1988).

[12] J. W. Oler and V. W. Goldschmidt, ''Coherent structures in the similarity region of two-dimensional turbulent jets,'' ASME J. Fluids Eng. **106**, 187 (1984).

[13] J. C. Mumford, ''The structure of the large eddies in fully developed turbulent shear flows. Part 1: the plane jet,'' J. Fluid Mech. **118**, 241 (1982).

[14] G. Urbin and O. Métais, ''Large-eddy simulations of spatially-evolving round jets: vortex control,'' Phys. Fluids (submitted).

[15] K. Akselvoll and P. Moin, ''Large-eddy simulation of turbulent confined coannular jets,'' J. Fluid Mech. **315**, 387 (1996).

[16] Y. Dai, T. Kobayashi, and N. Taniguchi, ''Investigation of organized structures in plane turbulent jet flow by using large eddy simulation,'' Proceedings, 10th Symposium on Turbulent Shear Flows, Vol. 1 (1995).

[17] C. Weinberger, J. Rewerts, and J. Janicka, ''The influence of inlet conditions on a large eddy simulation of a turbulent plane jet,'' Proceedings, 11th Symposium on Turbulent Shear Flows, Vol. 3 (1997).

[18] S. Stanley and S. Sarkar, ''A study of the flow field evolution and mixing in a planar turbulent jet using direct numerical simulation,'' J. Fluid Mech. (submitted).

[19] M. Lesieur and P. Comte, ''Large eddy simulation of compressible turbulent flows in turbulence in compressible flows,'' AGARD Report n819, pp. 4-1, 4-39 (1997).

[20] J. Smagorinsky, ''General circulation experiments with the primitive equations,'' Mon. Weather Rev. **91**, 99 (1963).

[21] B. Vreman, B. Geurts, and H. Kuerten, ''Large-eddy simulation of the turbulent mixing layer,'' J. Fluid Mech. **339**, 357 (1997).

[22] J. Bardina, J. H. Ferziger, and W. C. Reynolds, ''Improved turbulence models based on LES of homogeneous incompressible turbulent flows,'' Rep. TF-19, Department of Mechanical Engineering, Stanford (1984).

[23] L. Shao, S. Sarkar, and C. Pantano, ''On the relationship between the mean flow and subgrid stresses in LES of turbulent shear flows,'' Phys. Fluids **11**, 1229 (1999).

[24] M. Germano, U. Piomelli, P. Moin, and W. H. Cabot, ''A dynamic subgrid-scale eddy viscosity model,'' Phys. Fluids A **3**, 1760 (1991).

[25] B. Vreman, B. Geurts, and H. Kuerten, ''Comparison of numerical schemes in large eddy simulation of the temporal mixing layer,'' Int. J. Numer. Methods Fluids **22**, 297 (1996).

[26] S. Stanley and S. Sarkar, ''Simulations of spatially developing plane jets,'' AIAA 97-1922, 28th AIAA Fluid Dynamics Conference (1997).

[27] S. Stanley and S. Sarkar, ''Simulations of spatially developing two-dimensional shear layers and jets,'' Theor. Comput. Fluid Dyn. **9**, 121 (1997).

[28] S. K. Lele, ''Compact finite differences schemes with spectral like resolution,'' J. Comput. Phys. **103**, 16 (1992).

[29] M. H. Carpenter, D. Gottlieb, and S. Abarbanel, ''The stability of numerical boundary treatments for compact high-order finite-difference schemes,'' J. Comput. Phys. **108**, 272 (1993).

[30] K. W. Thompson, ''Time dependent boundary conditions for hyperbolic systems,'' J. Comput. Phys. **68**, 1 (1987).

[31] M. B. Giles, ''Nonreflecting boundary conditions for Euler equation calculations,'' AIAA J. **28**, 2050 (1990).

[32] D. H. Rudy and J. C. Strikwerda, ''A nonreflecting outflow boundary condition for subsonic Navier–Stokes calculations,'' J. Comput. Phys. **36**, 55 (1980).

[33] F. Q. Hu, ''On absorbing boundary conditions for linearized Euler equations by a perfectly matched layer,'' J. Comput. Phys. **129**, 201 (1996).

[34] J. W. Deardorff, ''On the magnitude of the subgrid scale eddy-viscosity coefficient,'' J. Comput. Phys. **7**, 120 (1971).

[35] S. Ghosal and P. Moin, ''The basic equations for large eddy simulation of turbulent flows in complex geometry,'' J. Comput. Phys. **118**, 24 (1995).

[36] B. J. Geurts, ''Inverse modeling for large-eddy simulation,'' Phys. Fluids A **9**, 3585 (1997).

[37] O. V. Vasilyev, T. S. Lund, and P. Moin, ''A general class of commutative filters for LES in complex geometries,'' J. Comput. Phys. **146**, 82 (1998).

[38] B. Vreman, ''Direct and Large Eddy Simulation of the compressible turbulent mixing layer,'' Ph.D. dissertation, University of Twente (1995).

[39] M. V. Salvetti and F. Beaux, ''The effect of the numerical scheme on the subgrid scale term in large-eddy simulation,'' Phys. Fluids A **10**, 3020 (1998).

[40] A. G. Kravchenko and P. Moin, ''On the effect of numerical errors in large eddy simulations of turbulent flows,'' J. Comput. Phys. **131**, 310 (1997).